PHYSICS OF FLUIDS **25**, 073301 (2013)

Dynamics of cavitation clouds within a high-intensity focused ultrasonic beam

Yuan Lu,[1] Joseph Katz,[1,a)] and Andrea Prosperetti[1,2]
[1]*Department of Mechanical Engineering, Johns Hopkins University, Baltimore, Maryland 21218, USA*
[2]*Faculty of Science and Technology, Impact Institute and J. M. Burgers Center for Fluid Dynamics, University of Twente, 7500 AE Enschede, The Netherlands*

(Received 11 June 2012; accepted 21 May 2013; published online 17 July 2013)

In this experimental study, we generate a 500 kHz high-intensity focused ultrasonic beam, with pressure amplitude in the focal zone of up to 1.9 MPa, in initially quiescent water. The resulting pressure field and behavior of the cavitation bubbles are measured using high-speed digital in-line holography. Variations in the water density and refractive index are used for determining the spatial distribution of the acoustic pressure nonintrusively. Several cavitation phenomena occur within the acoustic partially standing wave caused by the reflection of sound from the walls of the test chamber. At all sound levels, bubbly layers form in the periphery of the focal zone in the pressure nodes of the partial standing wave. At high sound levels, clouds of vapor microbubbles are generated and migrate in the direction of the acoustic beam. Both the cloud size and velocity vary periodically, with the diameter peaking at the pressure nodes and velocity at the antinodes. A simple model involving linearized bubble dynamics, Bjerknes forces, sound attenuation by the cloud, added mass, and drag is used to predict the periodic velocity of the bubble cloud, as well as qualitatively explain the causes for the variations in the cloud size. The analysis shows that the primary Bjerknes force and drag dominate the cloud motion, and suggests that the secondary Bjerknes force causes the oscillations in the cloud size. [http://dx.doi.org/10.1063/1.4812279]

I. INTRODUCTION

High-intensity focused ultrasound (HIFU), along with the associated cavitation, is used in a variety of fields. In medicine, research on, and applications of, HIFU have been expanding rapidly. Novel approaches to extracorporeal lithotripsy rely on HIFU rather than on shock waves, as the more traditional ones.[1–7] HIFU is also studied for use in conjunction with shock-wave lithotripsy in order to further reduce the fragments produced by that process.[8] These and related application fall under the broader category of histotripsy, in which acoustic cavitation is used for the precise mechanical fractionation of tissues, e.g., in cancer therapy.[9,10] Some of these applications involve frequencies in the range of 0.5–10 MHz, intensities in excess of 10^3 W/cm^2, and exposure durations of 1–30 s.[11] Many of these applications as well as others, including HIFU-induced cavitation for localized drug delivery, are reviewed by Coussios and Roy.[12] HIFU is also useful in many other applications such as sonochemistry, in which acoustic cavitation initiates and enhances chemical reactions (see, e.g., Refs. 13 and 14), acoustic cleaning and particle removal (see, e.g., Refs. 15 and 16), water treatment (see, e.g., Ref. 17), and many others.

When bubbles are in a non-uniform acoustic field, the spatial pressure gradient coupled with volumetric pulsations produce a net force, which is termed the primary Bjerknes force.[18] This acoustically generated force affects the bubble trajectories along with other hydrodynamic forces

a)Author to whom correspondence should be addressed. Electronic mail: katz@jhu.edu.

such as added mass, drag, etc.[19,20] During acoustic cavitation, clouds of bubbles often form, either directly or through fission of collapsing bubbles,[21] further complicating the understanding and modeling of the dynamics involved. Relative to the single bubble cases, studies focusing on the motion of cavitation clouds in HIFU fields are relatively limited. Willard[22] employed an intense, 2.5 MHz, focused acoustic beam, with pressure amplitude of up to 7 MPa, to study the resulting cavitation. He observed generation of plume-like bubble clouds moving at velocity of up to 10 m/s in both aerated and degassed water. The author suggested that the beam generated high-speed acoustic streaming in the liquid, which carried the clouds. He did not measure the liquid speed directly, but inferred it from the motion of microbubbles around the clouds. The measured velocity did not exceed 2 m/s, implying that other mechanisms must be involved in accelerating the clouds. Wu *et al.*[23] irradiated a cylindrical reactor with a 27.3 kHz, low level (maximum sound pressure of 100 kPa) unfocused ultrasonic beam, and observed that cavitation clouds could be generated in degassed water. The clouds traveled in the sound propagation direction toward the water-air interface at a velocity of up to 1 m/s.

The presence of neighboring boundaries with the associated reflected waves further complicates the dynamics of bubble clouds. Maxwell *et al.*[24] examined the formation of a cavitation cloud caused by 5–20, 1 MHz, high-amplitude cycles of ultrasound. Recording high-speed images at rates extending to 10^7 frames/s, they observed that clouds were initiated from a single cavitation bubble that formed during the initial cycles of the pulse, and then grew along the acoustic axis, in a direction opposite to the propagation direction. Finally, Arora *et al.*,[25] who are referred to later in this paper, investigated cavitation caused by a single HIFU cycle, and demonstrated the increase in extent and longevity of a cavitation cloud caused by artificially seeding the flow with microbubbles.

In the present study, we generate a HIFU beam in an otherwise quiescent water container with pressure amplitude of up to 1.9 MPa, and use high-speed digital in-line holography to measure the size, spatial distribution, and velocity of the bubbles. Furthermore, holography enables us to record the spatial variations of the water refractive index, thus demonstrating a novel experimental technique to visualize and quantify the acoustic field in the test chamber. The phenomena we describe are complex. In order to better understand them, we develop a model involving Bjerknes forces and attenuation of the sound field by the cloud. This model is able to predict the magnitude and spatial variations in cloud velocity reasonably well.

II. EXPERIMENTAL SETUP AND PROCEDURES

A. Facility and instrumentation

As illustrated in Fig. 1, most of the experiments described in this paper have been performed in a rectangular glass container with dimensions of 202 × 202 × 101 mm^3 containing tap water. This

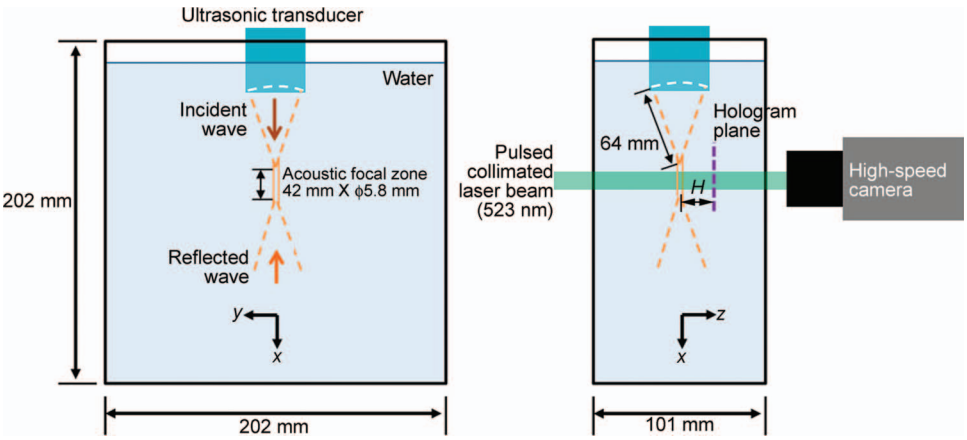

FIG. 1. Setups for the acoustic cavitation and high-speed digital in-line holography measurements. Reprinted with permission from Y. Lu, J. Katz, and A. Prosperetti, *Proceedings of the ASME 2012 Fluids Engineering Summer Meeting*. Copyright 2012 ASME.

chamber is open to the air on the top, and the water is initially quiescent. With a free interface, the water is most likely saturated with non-condensable gases. Furthermore, the tap water is not filtered and, consequently, most likely contains abundant cavitation nuclei. Indeed, the images described later revealed occasional presence of some <10 μm particles in the sample volume. The HIFU transducer, manufactured by Sonic Concepts, is positioned at the center of the top of the tank, with its radiating surface immersed in the water. This custom designed transducer operates at a fixed frequency $f = 500$ kHz, and has a maximum input power $P_{\text{in}} = 400$ W. The corresponding wavelength λ, for a sound speed c_0 of 1500 m/s in water at 20 °C, is 3 mm. The transducer has a concave radiating surface with diameter d_{rs} of 33 mm, which focuses the ultrasonic beam to a zone located 64 mm away from its surface. The focal zone is an approximately cylindrical volume with a diameter $d_{\text{f}} = 5.8$ mm and a length of 42 mm, as provided by the manufacturer and confirmed by our measurements (see below). The 500 kHz sinusoidal signal is generated using a function generator (Agilent Technologies, model No. 33220A). The signal is amplified by a 200 W RF power amplifier (Electronics & Innovation model No. 1020L), and monitored using a power meter (Sonic Concepts, model No. 22A). The signal is fed into a matching network, also manufactured by Sonic Concepts, and then into the transducer. At high power levels, the temperatures of the transducer itself and of the liquid in the focal zone increase rapidly. To prevent damage to the transducer and generation of thermally induced Rayleigh–Bénard convection in the liquid, the transducer was operated in a pulsed mode, each pulse lasting less than 2 s. The interval between two subsequent pulses was several minutes and long enough to allow the liquid to return to the quiescent condition. Every few pulses, the bubbles accumulating on the transducer's surface are removed to eliminate possible adverse effects on the ultrasonic waves.

A substantial fraction of the data acquisition about the bubble cloud characteristics as well as the sound field involves application of digital holography. Unlike conventional photography, a hologram is a record of the interference of the coherent light scattered from objects with a reference beam. Consequently, it not only contains information on light intensity propagating from illuminated objects, but also the phase of this light field.[27] Numerical reconstruction of the holograms at varying depths brings the objects, such as particles, bubbles, etc., into focus, enabling us to measure their size, shape, and spatial distribution.[28–33] For the present application, we employ digital in-line holography using the optical setup illustrated in Fig. 1. Due to the rapid motion of the bubble clouds (velocities of the order of m/s), the light source is a Q-switched pulsed 523 nm (green) laser (CrystaLaser), which generates up to 0.1 mJ/pulse, each with a duration of 10–20 ns, at a rate of up to 20 kHz. The laser beam is collimated and illuminates the volume of interest, mostly in the focal zone of the ultrasonic beam. The holograms are recorded using a high-speed CMOS camera (Photron FASTCAM-Ultima APX), which can record 2000 f/s at full resolution of 1024×1024 pixels and up to 30 000 f/s at a resolution of 256×128 pixels. The magnification varies from 1:1, for which the resolution is 17 μm/pixel, to 5:1, for which the resolution is 3.4 μm/pixel. Numerical reconstruction is performed using in-house developed software.[27] In addition to digital holography, we have also recorded images of the bubble fields using white light for illumination. The optical setup is identical to that shown in Fig. 1, except that the laser beam is replaced with a continuous incandescent light source. In this case, the exposure time can be controlled by the camera, but we have used full exposure times for images shown in this paper, i.e., $\sim$33 μs at 30 000 f/s, and $\sim$166 μs at 6000 f/s.

B. Visualization and measurement of the HIFU pressure field

This section describes the method used to visualize the pressure field and to quantitatively characterize the pressure in the focal zone of the ultrasonic beam. The pressure wave in the focal zone is nearly one-dimensional and can be expressed as

$$p(x, t) = p_0 + p'(x, t), \tag{1}$$

where p_0 and p' are the undisturbed and acoustic pressures, respectively. The acoustic pressure can be modeled as the sum of incident p'_{in} and reflected p'_{re} waves

$$p'(x, t) = p'_{\text{in}}(x, t) + p'_{\text{re}}(x, t) = p_{\text{f}} \sin(kx - \omega t) + C_{\text{R}} p_{\text{f}} \sin(kx + \omega t + \varsigma). \tag{2}$$

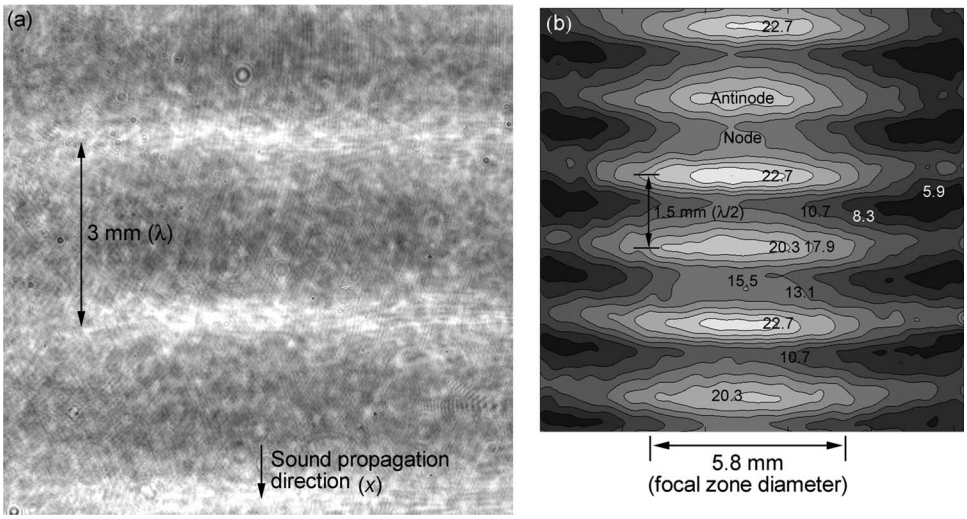

FIG. 2. Visualization and quantification of the focal zone of the ultrasonic wave; $p_f = 1.44$ MPa. (a) A sample hologram showing the instantaneous acoustic wave. The bright bands correspond to high pressure. (b) The distribution of the rms gray levels, showing the partial standing wave structure. Reprinted with permission from Y. Lu, J. Katz, and A. Prosperetti, *Proceedings of the ASME 2012 Fluids Engineering Summer Meeting*. Copyright 2012 ASME.

Here $k = 2\pi/\lambda$ is the wave number, $\omega = 2\pi f$ is the angular frequency, p_f is the amplitude of the incident wave, and ς is a phase lag. To account for the attenuation of the reflected wave and the defocusing of the reflected wave, we multiply its amplitude by a reflection coefficient C_R, $0 < C_R < 1$. The magnitude of p_f can be estimated from the input power and the efficiency ($\eta = 0.85$) of the HIFU system, as provided by the manufacturer. The resulting acoustic intensity at the transducer's radiating surface is $I_{rs} = \eta P_{in}/(\pi {d_{rs}}^2/4)$, and the acoustic pressure on the surface is $p_{rs} = (2I_{rs}Z)^{1/2}$, where Z is the acoustic impedance of water. The manufacturer specifies that the intensity gain in the focal zone is $g = 2.51$, and the incident pressure amplitude in the focal zone is therefore $p_f = gp_{rs}$. For example, at $P_{in} = 5$ W, $p_f = 306$ kPa, while at $P_{in} = 110$ W, $p_f = 1.44$ MPa, and at $P_{in} = 200$ W, $p_f = 1.94$ MPa.

One can also estimate the amplitude of the acoustic field from the changes to the water density. The substantial pressure fluctuations in the focal zone cause detectable variations in the density and the refractive index n of the water. When an initially collimated light beam passes through the spatially varying refractive index field, the beam alters its direction of propagation. Due to this angular deviation of the laser beam, the holograms formed on the focus plane of the imaging lens, placed at a distance H from the center of the acoustic focal zone, contain non-uniform shadowgraphic patterns. A sample hologram showing the instantaneous (averaged over the duration of the laser pulse of 10–20 ns) light intensity distribution for $P_{in} = 110$ W is presented in Fig. 2(a). The spatial intensity variations of the light field are related to the Laplacian of the refractive index on a plane normal to the light axis[34]

$$\frac{I'_{z=H}}{I_0} \triangleq \frac{I_{z=H} - I_0}{I_0} = -H \int_{-df/2}^{d_f/2} ({\nabla_\perp}^2 n) dz, \tag{3}$$

where I_0 is the undisturbed intensity and I is the intensity recorded at a distance z from the center of the acoustic beam (see Fig. 1). Assuming that the liquid density and refractive index vary mainly in the acoustic propagation direction, ${\nabla_\perp}^2 n$ is reduced to d^2n/dx^2 and $\int_{-d_f/2}^{d_f/2} ({\nabla_\perp}^2 n) dz = (d^2n/dx^2)d_f$. Using a first order approximation for $n = n(\rho)$, $d^2n/dx^2 = (dn/d\rho)(d^2\rho/dx^2)$. The quantity $dn/d\rho$ is a constant that can be determined from the Lorenz-Lorentz relation:[34]

$$\frac{n^2 - 1}{n^2 + 2} \frac{1}{\rho} = C, \tag{4}$$

where C is a constant that depends on the wavelength of the laser, properties of the liquid, temperature, and pressure. For a 523 nm laser wavelength at 20 °C and atmospheric pressure, $C = 2.1 \times 10^{-4}$ m^3/kg.[35] Finally, using a first order approximation, $p' = \rho' {c_0}^2$, the acoustic pressure can be expressed in terms of the light intensity

$$p'(x,t) = \frac{c^2}{(dn/d\rho)k^2 d_f H} \frac{I'(x,t)}{I_0}. \tag{5}$$

In the present experimental configuration, therefore, the acoustic pressure is proportional to the light intensity passing through the focal zone, and can be estimated from the distribution of light intensity (gray level) in the holograms. The bright bands indicate locally high pressure ($p' > 0$) since the light converges, and thus brighter ($I' > 0$) in regions of high refractive index [see Fig. 2(a)].

In a partially standing wave, there are no true pressure nodes since there are no points where the rms pressure p_{rms} is zero. However, for convenience, we still choose to call the regions with minimum p_{rms} as "nodes" and those with maximum p_{rms} as "antinodes." For the acoustic pressure field defined in Eq. (2), $p_{rms} = p_f\{0.5[1 + {C_R}^2 - 2C_R \cos(2kx + \varsigma)]\}^{1/2}$. The reflection coefficient can be obtained from $C_R = ({p_{rms}}^{max} - {p_{rms}}^{min}) / ({p_{rms}}^{max} + {p_{rms}}^{min})$, taking advantage of aliasing (variations in phase of instantaneous frames) caused by the mismatch between the acoustic frequency and sampling rate. Using Eq. (5), p_{rms} can be replaced with the rms gray level (I_{rms}) for each pixel, i.e.,

$$C_R = \frac{{I_{rms}}^{max} - {I_{rms}}^{min}}{{I_{rms}}^{max} + {I_{rms}}^{min}}. \tag{6}$$

The distribution of I_{rms} for $P_{in} = 110$ W is shown in Fig. 2(b), for which ${I_{rms}}^{max} = 21.7$, ${I_{rms}}^{min} = 13.1$, based on averaging along the central line of several antinodes and nodes, and thus $C_R = 0.25$.

Using C_R, I_{rms}, and d_f provided by the manufacturer, as well as Eq. (5), the estimated amplitude of the incident ultrasonic wave is $p_f = 1.32$ MPa. This result differs by about 10% from the previously mentioned amplitude calculated from information provided by the manufacturer ($p_f = 1.44$ MPa). Figure 2(b) also confirms that the width of the focal zone is consistent with the information provided by the manufacturer ($d_f = 5.8$ mm). The distribution the rms levels indicates that 2.9 mm from the center of the focal zone, the rms level is 6 dB below the peak level.

III. RESULTS

A. Annular bubble structures in the periphery of the focal zone

This paper deals primarily with cavitation in the focal zone of the transducer, the topic covered in Sec. III B. However, as background, it is of interest to summarize briefly the behavior of bubbles in the vicinity of, but outside, the focal zone as well. After being generated, bubbles subjected to acoustic excitation falling below the cavitation level are expected to grow by rectified diffusion.[36] Such gas bubbles cannot survive in the focal zone, where the acoustic pressure is too high.[37] Consequently, the phenomena described in this section occur *outside* of the focal zone at all transducer sound levels. Two sample images recorded at low sound levels, using white light, are presented in Fig. 3. Figure 3(a) is a vertical plane view showing that the bubbles accumulate in layers separated by λ/2 under the action of the primary Bjerknes forces. Figure 3(b) is a top (y-z) view showing that the bubbles are concentrated in circular ring surrounding, but clearly outside, the focal zone. This image was recorded in a smaller chamber during early experiments, in which the transducer was installed at the bottom of the facility, allowing observations from the top. The same phenomena occurred in the chamber illustrated in Fig. 1.

The resonant radius of gas bubbles at the transducer's frequency and atmospheric pressure is about 5.9 μm. This radius is smaller than that of the bubbles in Fig. 3(a) implying, on the basis of linear theory of the primary Bjerknes force, that the bubbles in this image are attracted to the nodes of the partial standing wave.[18] Furthermore, the secondary Bjerknes forces among these bubbles are attractive.[38] Therefore, adjacent bubbles tend to move toward each other, coalesce, and form bigger bubbles. These processes are evident in the high-speed movies, and the larger bubbles in Fig. 3(a),

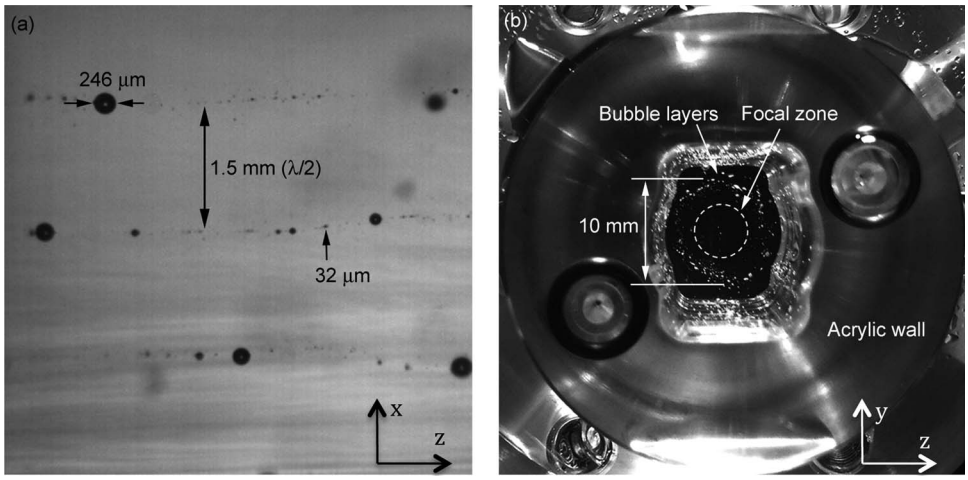

FIG. 3. (a) Annular bubble layers in the pressure nodes at low sound intensity ($p_f = 306$ kPa) recorded using white light illumination.[26] (b) A top-view of an early test chamber showing that the bubbles accumulate in the periphery of the focal zone (denoted with dashed circle). Reprinted with permission from Y. Lu, J. Katz, and A. Prosperetti, *Proceedings of the ASME 2012 Fluids Engineering Summer Meeting*. Copyright 2012 ASME.

which vary in size between 100 and 250 μm, are the result of the coalescence of several small ones. The secondary Bjerknes force also causes bubbles smaller than about 20 μm to rapidly jitter and orbit around bigger ones. When the sound is turned off, all the bubbles rise toward the free surface due to buoyancy.

B. Cloud cavitation

At high sound levels ($p_f \geq 1.2$ MPa), cavitation inception occurs near the axis of the acoustic beam, predominantly within, but also upstream of, the focal zone. The resulting bubble clouds, which are described below, travel at velocities of up to 4 m/s in the direction of the incident ultrasonic wave. This velocity is several orders of magnitude larger than the acoustically induced streaming, which was measured by tracking seeded micro-particles in the same facility, as well as by Particle Image Velocimetry (PIV) in the previously mentioned small chamber, which could be pressurized to prevent cavitation. These PIV measurements involved illumination of a non-cavitating focal zone with a pulsed Nd:YAG laser sheet, and seeding of the flow with 11 μm hollow glass spheres with a specific gravity of 1.1. The results, obtained using standard data analysis procedures,[39] revealed that acoustic streaming generated velocities ranging between 2 and 8 mm/s (not shown), orders of magnitude smaller than the cavitation bubble cloud velocity. We do not show these PIV results since they are not relevant to the phenomena described below.

Two examples of superpositions of high-speed images demonstrating the initial formation and migration of clouds for two sound levels are presented in Fig. 4. These images were recorded at 30 000 f/s, at a resolution of 256 × 128 pixel, using white light illumination, and frames were super-imposed without any additional processing, enhancement, or relative translation (except for trimming their sides). In each original frame, the cloud appears once, and the superposition shows the location and changes in size of the same cloud as it progresses along the direction of the ultrasonic beam. The top cavitation "blob" in each image shows how the cavitation appears in the first frame in which it becomes visible. Once cavitation inception occurs, the cavitation persists, namely, the cloud does not disappear for periods that vary between hundreds to thousands of acoustic cycles. In Figs. 4(a) and 4(c) we omit some of the frames (but not the first one) to make the ones displayed clearer, whereas the corresponding Figs. 4(b) and 4(d) contain all the frames with cavitation until the cavitation cloud leaves the field of view. In the following description, we separate the discussion on the appearance of cavitation at moderate pressures, of which Figs. 4(a) and 4(b) are representatives, and at high pressures, of which Figs. 4(c) and 4(d) are representative.

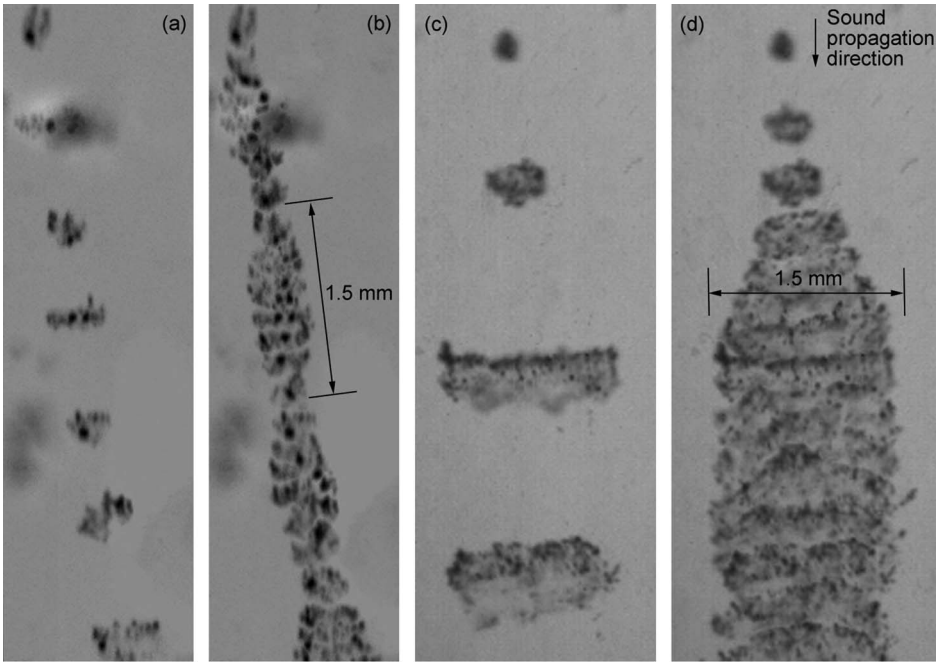

FIG. 4. Superpositions of time series of sample bubble clouds recorded using white light at (a) and (b) high sound level ($p_f = 1.44$ MPa), where the speed and diameter of the cloud are periodic, with (a) showing a few samples and (b) containing the entire series; (c) and (d) very high sound level ($p_f = 1.89$ MPa), where the cloud becomes large, travels at almost a constant velocity, and maintains constant diameter after the initial growth phase. Here (c) shows a few samples and (d) the entire series.

The inception of cavitation at $p_f = 1.44$ MPa, included in Figs. 4(a) and 4(b), involves the intermittent explosive creation of a nearly spherical compact volume of microbubbles with an overall size of about 200 μm, and rapid expansion of this cloud in the horizontal direction to form a migrating layer. The location and timing of inception vary, presumably due to the specific position of cavitation nuclei, but it mostly occurs in the vicinity of the pressure antinodes. The inception occurs over a time scale much shorter than that resolved by our fastest image acquisition rate of 30 000 f/s, i.e., in less than 33 μs. In other words, within our resolution limit, there is no evidence that cavitation is about to occur in frames preceding the one shown at the top of Fig. 4. The same observation applies to the holographic images at a slower frame rate (2000 f/s), which have a resolution of 3.4 μm/pixel and, therefore, a lower limit on the diameter of readily resolvable bubbles of about 10 μm (3 pixels). Even when the cloud moves, the velocity of the liquid surrounding it remains very low, except for the regions directly affected by the cloud-induced motion, e.g., its wake. Thus, consistent with the observations by Willard,[22] the bubble cloud motion is not induced by acoustic streaming. After a few clouds are generated, the surrounding flow field is sufficiently disturbed that the bubbly rings surrounding the focal zone shown in Fig. 3(b) are destroyed. Turning the sound off makes the cloud disappear in less than 33 μs, leaving no noticeable traces, again within our resolution limit of about 10 μm diameter.

A typical close-up holographic view of an instantaneous cavitation bubble cloud during the translation phase (i.e., not the initial cluster) is presented in Fig. 5. In this image, to show in focus micro-bubbles located at different depths, we "collapse" (superimpose) a series of adjacent reconstructed planes onto a single image. Thus, the bubbles shown are actually located at different depths, the sum total of which is comparable with the horizontal extension shown in the image. As is evident, the typical radius r is about 20 μm, but the size of the bubbles varies, and some of them are at least twice as large. As noted above, when the sound is turned off, the bubbles disappear (i.e., fall below our resolution limit) within a time shorter than one inter-frame delay. Thus, the radius of bubbles decreases by at least 4 times, and their volume by 64 times when the sound is turned

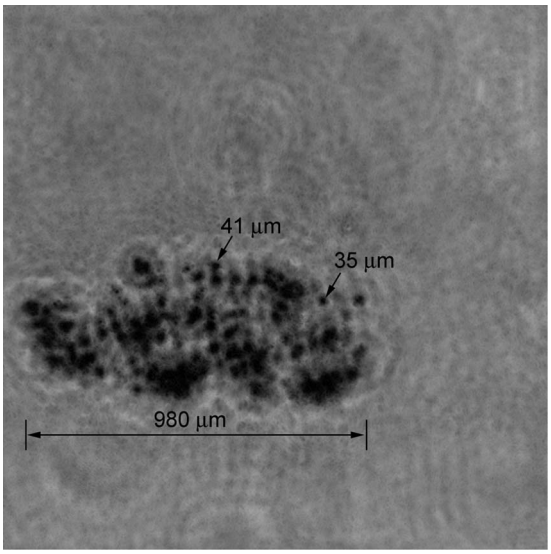

FIG. 5. A close-up view of the inner structure of a bubble cloud; $p_f = 1.44$ MPa. This picture is generated by collapsing a series of reconstructed holograms from different depths onto a single plane.

off. It may therefore be estimated that the volume fraction of non-condensable gas in the bubbles during the acoustic radiation is less than 1/64 (∼2%). This estimate neglects the mass diffusion of non-condensable gas out of the bubble between exposures, whose dissolution would take a longer time. This observation confirms that the bubbles in the cloud contain very little non-condensable gas. These bubbles, therefore, contain mostly water vapor. Consequently, in Secs. IV and V, in which we develop a model for the behavior of the cloud, we assume that the bubbles within the cavitation cloud contain only vapor. However, these bubbles do not collapse/disappear completely during the compression phase as long as the sound is turned on, presumably since the short duration of compression (2 μs) prevents them from condensing completely, allowing them to actually grow in subsequent cycles. In contrast, the bubbles within the rings surrounding the acoustic focal zone (Sec. III A), which grow by rectified diffusion, contain mostly non-condensable gas. Accordingly, they do not disappear when the sound is turned off and rise by buoyancy.

In general, the cloud size increases with acoustic pressure and its dynamics are found to be correlated with its diameter and location relative to the sound field. When $p_f < 1.68$ MPa, the characteristic diameter of the cloud is smaller than $\lambda/3$. In this case, the cloud periodically expands while decelerating and contracts while accelerating. These size variations are evident in Figs. 4(a) and 4(b). Quantitative examples of the changes in velocity and cloud size during the translation phase are provided in Fig. 6. Figures 6(a) and 6(b) present two series of reconstructed holographic images of clouds, highlighting the changes in their size and location relative to the nodes and antinodes of the acoustic field. Here, the progression of the two clouds is presented in separate frames showing the location and timing of each image. Both clouds slow down and increase in size near the nodes of the partial standing wave, as well as accelerate and shrink in the vicinity of the antinodes. Corresponding information on the cloud velocity and diameter is provided in Figs. 6(c) and 6(d). On the other hand, once formed, the thickness of the clouds fluctuates, but does not show a clear correlation with the structure of the partial standing wave. Increasing the magnification of the holograms enables us to resolve the spatial distribution of bubbles within the cloud, as illustrated before in Fig. 5.

For $p_f \geq 1.68$ MPa, e.g., $p_f = 1.89$ MPa, cavitation inception still appears as a ∼200 μm cluster of bubbles, as the top images in Figs. 4(c) and 4(d) demonstrate. Subsequently, the diameter of some of the clouds becomes comparable and even larger than $\lambda/2$, and they appear as flat disks with varying thickness. In this case, after the initial growth phase, once the cloud reaches its maximum size, its speed and diameter do not change significantly. The unreconstructed (i.e., original) hologram in Fig. 7 is an extreme example of a flattened thin layer of cavitation bubbles at high sound levels,

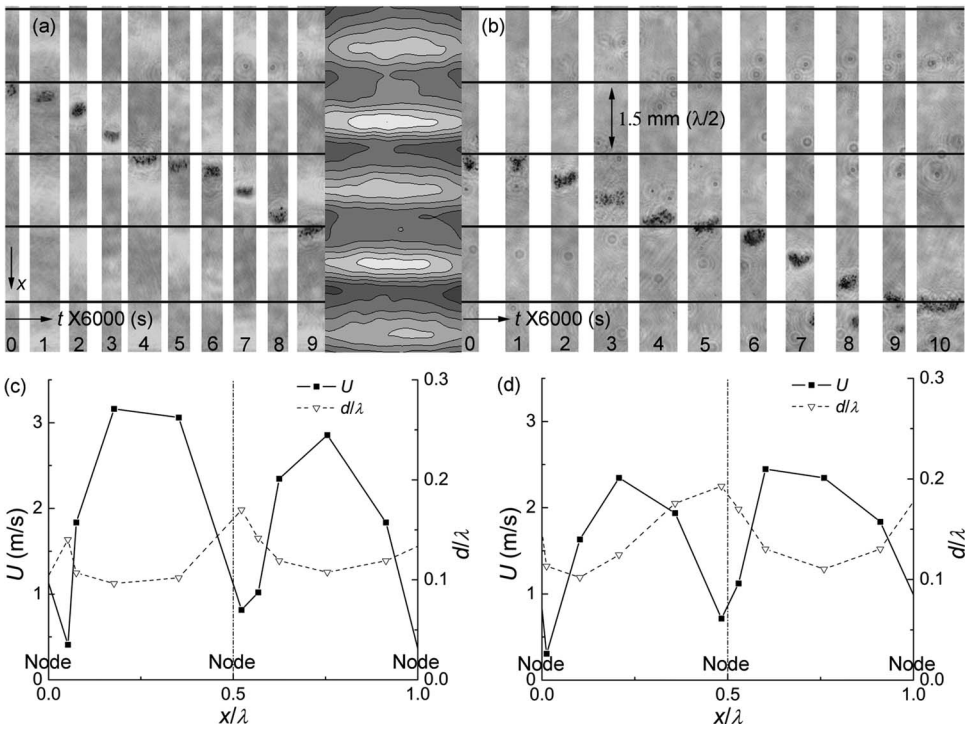

FIG. 6. (a) and (b) Time series of reconstructed holograms ($\Delta t = 167$ μs) showing the axial locations of two sample bubble clouds in a motion cycle, and the corresponding location of the pressure nodes (thick solid-lines) determined from the distribution of rms pressure levels; $p_f = 1.44$ MPa. (c) and (d) Corresponding velocity and diameter vs. the cloud location in a motion cycle. Parts (a) and (c) are reprinted with permission from Y. Lu, J. Katz, and A. Prosperetti, *Proceedings of the ASME 2012 Fluids Engineering Summer Meeting*. Copyright 2012 ASME.

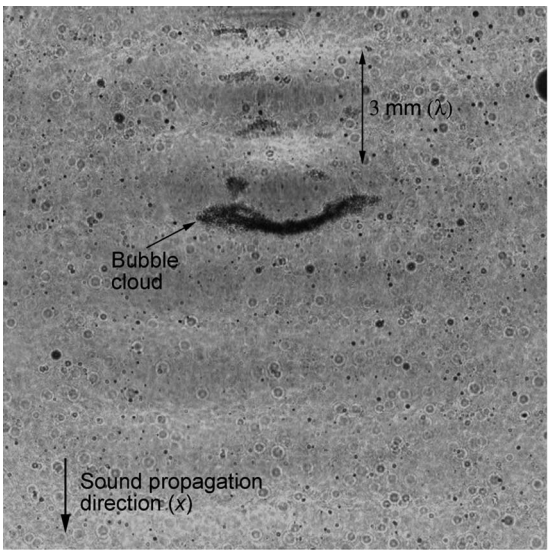

FIG. 7. A sample original instantaneous hologram showing the reflection of the incident acoustic wave by a large bubble cloud; $p_f = 1.89$ MPa. The wave on the leeward side of the cloud becomes nearly invisible. The bubbles that are out of focus can be seen in the background.

with a diameter as large as λ. We present an original hologram to show the cloud shape as well as the signature of the acoustic field. Here, the amplitude of the acoustic wave on the "leeward" side of the cloud is much weaker than that on its "windward" side. This observation indicates that there is little transmission of sound through the cloud. Furthermore, the amplitude of the wave on the acoustic windward side appears to be higher than that in the surrounding fluid, suggesting a partial reflection of the sound wave, which constructively interferes with the incident wave. These trends imply that the weakening of the sound transmission eliminates the partial standing wave, and with it, the periodic variations in the cloud size and velocity. To confirm this statement, we covered the bottom of the test chamber with fiber bristles in order to attenuate the sound reflection. Indeed, irrespective of the incident sound level, the periodic variations in the cloud velocity and size disappeared, supporting our hypothesis that both of them are caused by the partial standing wave. In Secs. IV and V, we develop a model that explains the periodic behavior of the bubble clouds.

Several comments should be made before concluding this observation section: First, like most cavitation phenomena, the onset of cavitation depends on the presence of cavitation nuclei. We did not measure the nuclei concentration, but since our experiments were performed using tap water saturated with non-condensable gases, this water was most likely rich with nucleation sites. However, one should keep in mind that the "strength" of the water increases with frequency, and only micron size bubbles would become active at a frequency of 500 kHz. This fact may explain the intermittent occurrence of cavitation inception in our experiments in spite of the high pressure peaks. Second, phenomena relevant to the present findings were reported by Arora *et al.*[25] They investigated cavitation caused by a single pulse involving ∼10 MPa tension for ∼2 μs, with and without artificial seeding of nuclei—phospholipid shelled, 2.5 μm diameter bubbles, and in water degassed to 30% of the saturation level. The amplitude of the present pressure pulses was 5–7 times smaller, but the cycle duration was comparable. They also showed that cavitation was confined to the focal zone of the acoustic beam irrespective of the nuclei concentration. Without artificial seeding, few traces of their bubble cloud remained after 165 μs, and they disappeared completely after 265 μs. This rapid cloud disappearance was consistent, at least to within an order of magnitude, with the present observations, in which the cloud disappeared after 33 μs, presumably due to the marked differences in amplitude. To achieve cavitation that persisted for longer periods, Arora *et al.* had to introduce the abovementioned artificial nuclei. Their measurements confirmed that the spatial extent within the focal zone, concentration, and "longevity" (duration of time that they existed after the shock) of the cavitation increased substantially upon introduction nuclei.

IV. A MODEL FOR THE AXIAL MOTION OF THE BUBBLE CLOUD

The cloud appears as a pancake-like mixture of bubbles and water, with volume of $V = \pi R^2 S$, where R and S are its radius and thickness, respectively. However, some of its features are more easily estimated by approximating it as a sphere with an equivalent radius of $R_e = (3S/4R)^{1/3}R$. The velocity of the cloud is three orders of magnitude lower than the speed of sound in water, i.e., the associated time scales are very different. Consequently, it is reasonable to perform an analysis of the cloud dynamics, averaging over many acoustic cycles, but allowing time and cloud properties to vary on the time scale of cloud translation. The motion of the cloud is assumed to be one-dimensional, along the direction of sound propagation. In addition, we assume that the cloud contains uniformly distributed bubbles that are much smaller than the cloud size, and consequently, we treat it as a homogeneous medium. Internal interactions among the bubbles, e.g., by secondary Bjerknes forces, are also neglected. Gravity is neglected, consistent with its small magnitude relative to the acoustic pressure gradients. Subject to these assumptions, an equation of motion for the cloud can be formulated by combining the forces associated with its translation, namely added mass and drag, with the acoustic forces, i.e., the primary Bjerknes force and the force resulting from loss of momentum of the acoustic beam due to attenuation

$$\bar{F}_{PB} + \bar{F}_{Att} + \bar{F}_{D} + \bar{F}_{AM} = \bar{\rho}_m \bar{V} \ddot{x}, \tag{7}$$

where the overbar denotes time averaging, dots denote time derivatives with respect to the cloud time scale, $\bar{F}_{PB}$ is the primary Bjerknes force, $\bar{F}_{Att}$ is the propulsive force due to sound attenuation in

the cloud, $\bar{F}_{\rm D}$ is the drag, $\bar{F}_{\rm AM}$ is the force due to added mass, $\bar{\rho}_{\rm m} = (1-\bar{\varphi})\,\bar{\rho} + \bar{\varphi}\,\bar{\rho}_{\rm V} \approx (1-\bar{\varphi})\,\bar{\rho}$ is the density of the bubbly mixture, $\bar{\varphi}$ is the time averaged vapor volume fraction, and $\bar{\rho}$ and $\bar{\rho}_{\rm V}$ are the time averaged densities of water and vapor, respectively. For the present measurements, $\bar{\varphi}$ is about 1%. For such a volume fraction, the buoyancy force is two orders of magnitude smaller than the other contributions, and it is neglected. With expressions for all the forces, we obtain a second order ordinary differential equation for the cloud displacement, and then solve it numerically.

The primary Bjerknes force on the cloud is[18]

$$F_{\rm PB} = -\overline{V'\partial_x p'}, \tag{8}$$

where the apostrophe denotes the oscillatory part of the relevant quantities. For simplicity, we assume small oscillations of the cloud size, and estimate V' by using a spherical model, in which R'_e is calculated from the linearized Rayleigh-Plesset equation[40]

$$\ddot{R}'_e + 2\beta\dot{R}'_e + \Omega_r^2 R'_e = -\frac{p'}{\bar{\rho}\bar{R}_e}, \tag{9}$$

where β and $\Omega_{\rm r}$ are the damping coefficient and resonant frequency of the cloud, respectively, and are functions of x. Use of the linearized Rayleigh-Plesset equation might not be appropriate for isolated cavitation bubbles that are expected to vary in size by orders of magnitude.[41] However, as the data show, the variations in the overall cloud dimensions are very small during the acoustic cycles, as witnessed by ensemble of holograms collected at different phases. Consequently, basing the analysis on the linearized equation to explain trends is justified. Substituting the pressure fluctuations associated with the partial standing wave [Eq. (2)], we obtain

$$\begin{aligned} R'_{\rm e} = &-\frac{p_{\rm f}}{\bar{\rho}\bar{R}_{\rm e}\omega^2\left\{\left[\left(\frac{\Omega_{\rm r}}{\omega}\right)^2-1\right]^2+4\left(\frac{\beta}{\omega}\right)^2\right\}} \\ &\times\left\{\left[\left(\frac{\Omega_{\rm r}}{\omega}\right)^2-1\right]\left[\sin(kx-\omega t)+C_{\rm R}\sin(kx+\omega t+\varsigma)\right]\right. \\ &\left.+2\left(\frac{\beta}{\omega}\right)\left[\cos(kx-\omega t)-C_{\rm R}\cos(kx+\omega t+\varsigma)\right]\right\}. \end{aligned} \tag{10}$$

With $V' \approx 4\pi\bar{R}_{\rm e}^2 R'_{\rm e}$, the primary Bjerknes force (8) becomes

$$\bar{F}_{\rm PB} = \frac{4\pi k\bar{R}_{\rm e}{p_{\rm f}}^2}{\bar{\rho}\omega^2\left\{\left[\left(\frac{\Omega_{\rm r}}{\omega}\right)^2-1\right]^2+4\left(\frac{\beta}{\omega}\right)^2\right\}}\left\{C_{\rm R}\left[\left(\frac{\Omega_{\rm r}}{\omega}\right)^2-1\right]\sin(2kx+\varsigma)+\left(1-{C_{\rm R}}^2\right)\frac{\beta}{\omega}\right\}. \tag{11}$$

The first term in this expression is associated with the partial standing wave, and oscillates with a spatial period of $\lambda/2$. Since $\Omega_{\rm r} < \omega$, as shown below, this contribution is always directed toward the pressure nodes. The second term corresponds to the propagating part of the wave due to the partial reflection of the incident wave. This part of the force always points in the direction of the incident wave.

To obtain $\Omega_{\rm r}$ for the cloud, we use the result of a linear analysis, which shows that a spherical bubble cloud has a series of resonance frequencies[42]

$$\Omega_r = \omega_r \Bigg/ \left[1+\frac{3\bar{\varphi}(1-\bar{\varphi})}{(j-1/2)^2\pi^2}\left(\frac{\bar{R}_e}{\bar{r}}\right)^2\right]^{-0.5}, \tag{12}$$

where $j = 1, 2, 3, \ldots$, $\omega_{\rm r}$ is the resonant frequency of an individual bubble, and $\bar{r}$ is its mean radius, which is 29 μm for the present measurements. Although this equation was originally developed for clouds consisting of gas bubbles, it can readily be shown to be applicable for the case of vapor bubbles provided that $\omega_{\rm r}$ is the natural frequency of a single vapor bubble. Since the lowest mode is dominant,[42] we will use $\Omega_{\rm r} = \Omega_1$. Note that $\Omega_{\rm r}$ is always smaller than $\omega_{\rm r}$.

The damping coefficient β can be estimated by relating the cloud properties to those of the individual bubbles through the compressibility of the mixture $K_{\rm m} = (\rho_{\rm m}c_m^2)^{-1} \approx \left[(1-\bar{\varphi})\bar{\rho}c_m^2\right]^{-1}$, where $c_{\rm m}$ is the speed of sound within the cloud. By definition, $k_{\rm m} = -(1/V)(dV/dp)$

$= -(3/\bar{R}_e)(dR'_e/dp')$, and dR'_e/dp' can be obtained from the solution to Eq. (9), $R'_e = -p' \Big/ \left\{\bar{\rho}\bar{R}_e\omega^2\left[\left(\frac{\Omega_r}{\omega}\right)^2 - 1 + i2\left(\frac{\beta}{\omega}\right)\right]\right\}$, where $i = \sqrt{-1}$. By taking the real part [denoted with $\Re\{\}$] of dR'_e/dp', we have

$$K_m = -\frac{3}{\bar{R}_e}\Re\left\{\frac{dR'_e}{dp'}\right\} = \frac{3\left[\left(\frac{\Omega_r}{\omega}\right)^2 - 1\right]}{\bar{\rho}\bar{R}_e{}^2\omega^2\left\{\left[\left(\frac{\Omega_r}{\omega}\right)^2 - 1\right]^2 + 4\left(\frac{\beta}{\omega}\right)^2\right\}}. \tag{13}$$

The complex sound speed in a bubbly mixture containing either gas or vapor bubbles is given by[43]

$$\frac{1}{c_m^2} = \frac{1}{c_0^2} + \frac{3\bar{\varphi}}{\bar{r}^2\omega^2\left[\left(\frac{\omega_r}{\omega}\right)^2 - 1 + i2\left(\frac{b}{\omega}\right)\right]}, \tag{14}$$

where b is the damping coefficient of an individual bubble. Since $(1-\bar{\varphi})\bar{\rho}K_m \approx \Re\left\{1/c_m^2\right\}$,

$$\beta = \frac{\omega}{2}\left\{\frac{3(1-\bar{\varphi})\left(\frac{\bar{r}}{\bar{R}_e}\right)^2}{\left(\frac{\bar{r}\omega}{c_0}\right)^2 \Big/ \left[\left(\frac{\Omega_r}{\omega}\right)^2 - 1\right] + 3\bar{\varphi} \Big/ \left(\left[\left(\frac{\omega_r}{\omega}\right)^2 - 1\right]^2 + 4\left(\frac{b}{\omega}\right)^2\right)} - \left[\left(\frac{\Omega_r}{\omega}\right)^2 - 1\right]^2\right\}^{1/2}. \tag{15}$$

The expressions of ω_r and b of a linearly oscillating vapor bubble are provided in Ref. 44:

$$\omega_r = \left[\frac{1}{\bar{\rho}\bar{r}^2}\left(3\frac{\Re\{K\} - B\Im\{K\}}{|K|^2} - \frac{2\sigma}{\bar{r}}\right)\right]^{1/2} \tag{16}$$

and

$$b = \frac{3}{2\omega\bar{\rho}\bar{r}^2}\frac{\Im\{K\} + B\Re\{K\}}{|K|^2}, \tag{17}$$

where $\Im\{\}$ denotes the imaginary part, σ is the surface tension, and K is the complex compressibility of a vapor bubble

$$\begin{aligned} K = {} & \frac{1}{\gamma\bar{p}_b} \\ & + 3\frac{c_s}{L}\left(\frac{\gamma-1}{\gamma}\frac{\bar{T}_s}{\bar{p}_b} - \frac{dT_s}{dp}\right)\left[\frac{D_v}{i\omega\bar{r}^2} - \sqrt{\frac{D_v}{i\omega\bar{r}^2}}\coth\left(\sqrt{\frac{i\omega\bar{r}^2}{D_v}}\right)\right] \\ & - \frac{i3\kappa_w}{\bar{\rho}_v L\omega\bar{r}^2}\left(1 + \sqrt{\frac{i\omega\bar{r}^2}{D_w}}\right)\frac{dT_s}{dp}, \end{aligned} \tag{18}$$

$$B = \frac{2\kappa_w}{\bar{\rho}_v L D_w}\frac{dT_s}{dp}\frac{2D_w}{\omega\bar{r}^2}\left(p_0 - \bar{p}_V + \frac{2\sigma}{\bar{r}}\right)\left[1 - 3G\left(\sqrt{\frac{\omega\bar{r}^2}{2D_w}}\right)\right], \tag{19}$$

and

$$G(w) = w^4\int_0^\infty \frac{\exp[-(1+i)s]}{(w+s)^5}ds. \tag{20}$$

In the above expressions, γ is the ratio of the specific heats, c_s is the specific heat of the vapor along the saturation line, L is the latent heat, $\bar{T}_s$ is the mean temperature at the vapor-water interface, $\bar{p}_b$ is the mean pressure in the bubble, $dT_s/dp \approx \bar{T}_s/(L\bar{\rho}_V)$, D_V and D_W are the thermal diffusivity of vapor and water, respectively, κ_W is the thermal conductivity of water, and Δp is the difference between the liquid static pressure and the saturation pressure. For the current case, $2D_W/(\omega\bar{r})^2 = 2.2 \times 10^{-4}$, which is much smaller than unity. As a result, B is negligible and the calculation can

be greatly simplified.[44,45] Using the current parameters, $\omega_r = 0.12\omega$ and $b = 0.072\ \omega$, and as a result, Ω_r [Eq. (12)] is at least an order of magnitude smaller than ω. All the terms needed for calculating β [Eq. (15)] and $\bar{F}_{PB}$ [Eq. (11)] are now available.

Next, we estimate the propulsive force due to sound attenuation in the cloud, $\bar{F}_{Att}$. Attenuation of sound in bubble clouds has been investigated extensively.[43,46] Such attenuation causes streamwise gradients in the associated normal Reynolds stress and, consequently, a streamwise force, much like in acoustic streaming.[47,48] For a bubbly cloud, the magnitude of this force is

$$\bar{F}_{Att} = \pi \bar{R}^2 \bar{\rho} \Delta \overline{u'^2}. \tag{21}$$

Here u' is the acoustically induced liquid velocity and Δ denotes the difference across the cloud. For a linear acoustic wave, the velocity fluctuation on the acoustic windward side of the cloud is $u'_{wind} = \left[p'_{in} - p'_{re}\exp(-\alpha S)\right]/(\bar{\rho}c_0)$, and on the leeward side is $u'_{lee} = \left[p'_{in}\exp(-\alpha S) - p'_{re}\right]/(\bar{\rho}c_0)$, where α is the attenuation coefficient across the cloud. In this estimate, we assume that the cloud is small enough that the local sound diffraction by it does not affect the overall strength of the reflected wave. Substituting Eq. (2) for the pressure, and time averaging, we obtain

$$\bar{F}_{Att} = \frac{\left(1 - e^{-2\alpha\bar{S}}\right)\left(1 - C_R^2\right) p_f^2 \pi \bar{R}^2}{2\bar{\rho}c_0^2}. \tag{22}$$

The attenuation coefficient is calculated from the complex sound speed in a bubbly mixture[29]

$$\alpha = -\omega \Im\left\{\frac{1}{c_m}\right\}. \tag{23}$$

Using Eq. (14), and the present conditions, we obtain $\alpha = 8.47 \times 10^3$ 1/m and $\exp(-\alpha S) = 0.034$ for a characteristic cloud thickness of 200 μm, so that the wave is substantially attenuated across the cloud.

The drag force on the cloud is

$$\bar{F}_D = -\tfrac{1}{2} C_D \bar{\rho} \pi \bar{R}^2 \dot{x}^2, \tag{24}$$

where C_D is the drag coefficient. For a wide range of Reynolds numbers, the drag coefficient of a circular disk is essentially unity.[49] Finally, we estimate the force due to the added mass by simply assuming that the cloud is a sphere with an equivalent radius, i.e.,

$$\bar{F}_{AM} = -\bar{m}_{add}\ddot{x} = -\tfrac{2}{3}\bar{\rho}\pi \bar{R}_e^3 \ddot{x}. \tag{25}$$

Use of an added mass for a thin disk with the same radius R, which would over-estimate the added mass, would about double this force.[50] Using the derived expressions for the forces, and a change of variables to $X = x + \frac{\varsigma}{2k}$ in order to eliminate the irrelevant phase lag ς, we obtain the following nonlinear second order differential equation:

$$\begin{aligned}\ddot{X} = &-\frac{C_D}{2(1.5 - \bar{\varphi})\bar{S}}\dot{X}^2 \\ &+\frac{4k p_f^2 \bar{R}_e}{(1.5 - \bar{\varphi})\bar{\rho}^2\omega^2\bar{R}^2\bar{S}}\frac{C_R\left[\left(\frac{\Omega_r}{\omega}\right)^2 - 1\right]\sin X + \left(1 - C_R^2\right)\beta/\omega}{\left\{\left[\left(\frac{\Omega_r}{\omega}\right)^2 - 1\right]^2 + 4\left(\frac{\beta}{\omega}\right)^2\right\}} \\ &+\frac{\left(1 - e^{-2\alpha\bar{S}}\right)\left(1 - C_R^2\right) p_f^2}{2(1.5 - \bar{\varphi})\bar{\rho}^2 c_0^2 \bar{S}}.\end{aligned} \tag{26}$$

To estimate the cloud motion, we use the experimental observation that $\bar{R}(X)$ oscillates nearly harmonically in space and, as a result, we estimate it as $\bar{R}(X) = 0.5\left[\left(\bar{R}_{max} - \bar{R}_{min}\right)\cos 2kX + \left(\bar{R}_{max} + \bar{R}_{min}\right)\right]$. Based on the average dimensions of 30 clouds, we use $\bar{R}_{max} = 350$ μm and $\bar{R}_{min} = 100$ μm as the characteristic maximum and minimum radius, respectively. The thickness does not show a clear correlation with the partial standing wave, and

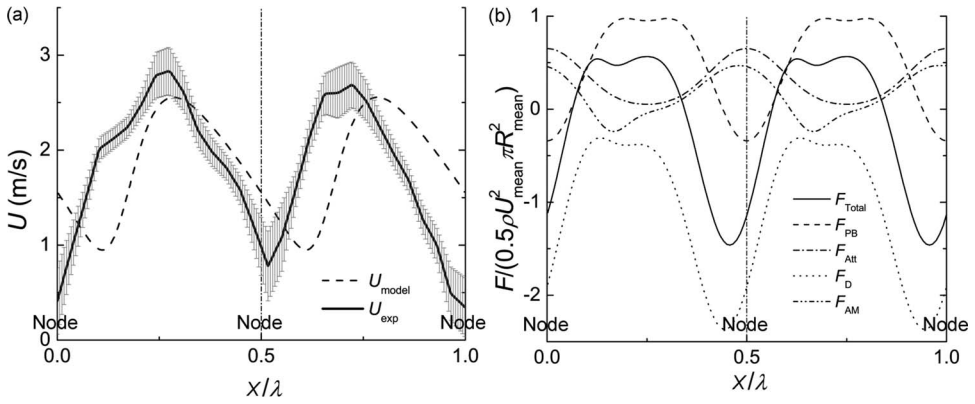

FIG. 8. (a) A comparison between the measured and predicted [Eq. (26)] bubble cloud velocity. The error bars indicate the standard deviation of the measured values. (b) The predicted total force and its components; $p_f = 1.44$ MPa.

seems to fluctuate about some mean value. For the calculation, we use the average thickness of the 30 clouds, $\bar{S} = 200\ \mu$m. With the initial conditions $X(0) = \lambda/4,\ \dot{X}(0) = 0$, since cavitation inception typically occurs in the pressure antinodes, Eq. (26) is solved using the MATLAB solver "ode45." Figure 8(a) shows the "steady-state" solution for $p_f = 1.44$ MPa, and compares it to the measured cloud velocity averaged over 30 clouds. The model reproduces the correct magnitude of cloud velocity, but there is a phase difference. In the case of a big cloud ($\bar{R} = 1.5$ mm, $p_f = 1.89$MPa), for which $C_R = 0$, the model predicts a constant steady-state velocity of 1.36 m/s (after the initial acceleration), which is 12% lower than the averaged observed value (1.54 m/s).

Figure 8(b) shows the variations of calculated forces normalized using the predicted mean velocity and characteristic mean radius. In the vicinity of the nodes the total force is negative, and thus decelerating the cloud there. The primary Bjerknes force and the drag contribute to this deceleration, while the attenuation force and added mass are positive. Although the latter are small, without the attenuation and added mass, the cloud would not have enough inertia to escape from the nodes, and would be trapped there. Near the antinodes, the primary Bjerknes force propels the cloud. Before concluding this section, it should be noted that we have performed the previous analysis also for a cylindrical cloud with the measured radius and height. It adds extra complexity to the expressions involved, but does not alter the predicted trends so significantly to warrant presentation of both results.

V. MECHANISMS AFFECTING THE BUBBLE CLOUD SIZE

In Sec. IV, the measured variations in cloud size were used as an input. In this section, we discuss possible mechanisms affecting the periodic contraction and expansion of the smaller clouds. In general, one would expect that once cavitation inception occurs, persistent exposure to the acoustic field would increase the cavitation activity, as the bubbles collapse and fragment, thus increasing the nuclei population. In contrast, the observed spatial extent of the cloud remains confined and, furthermore, it shrinks near the pressure antinodes, where the pressure fluctuations peak. A possible mechanism for these trends involves interactions among bubbles, such as the secondary Bjerknes force,[38] namely, the force on a bubble resulting from the pressure field generated by volume oscillations of all the other bubbles in a cloud.

It is well known that the secondary Bjerknes force between two equal bubbles, according to linear theory, is attractive both when the bubbles are driven above and below the resonance frequency. The theory gives this force in the form[38]

$$\bar{F}_{SB} = -\frac{\bar{\rho}}{4\pi \bar{l}^2}\overline{\dot{v}_1' \dot{v}_2'}, \tag{27}$$

where v_1' and v_2' are the oscillating bubble volumes, and l is the distance between them. To estimate this force, we assume that the two bubbles have the same equilibrium radius, which is larger than the

resonant size, and that they are subjected to the pressure expressed in Eq. (2). Solving the linearized Rayleigh-Plesset equation[40] for each bubble to estimate the volume oscillations gives

$$\bar{F}_{\mathrm{SB}} = -\frac{2\pi \bar{r}^2 p_{\mathrm{f}}^2}{\bar{\rho}\omega^2 \bar{l}^2 \left(\left[\left(\frac{\omega_{\mathrm{r}}}{\omega}\right)^2 - 1 \right]^2 + 4\left(\frac{b}{\omega}\right)^2 \right)} \left(-2C_{\mathrm{R}} \cos X + {C_{\mathrm{R}}}^2 + 1 \right). \tag{28}$$

As is evident, $\bar{F}_{\mathrm{SB}}$ is negative, i.e., it is an attractive force.[26] However, its magnitude peaks at the antinodes, where the pressure oscillation peaks, and is minimal at the nodes. Thus, the bubbles within the cloud are more likely to form dense clusters in the vicinity of the antinodes. The magnitude of the secondary Bjerknes force can be of the same order as the primary Bjerknes force, especially when many bubbles are involved. Thus, the influence of $\bar{F}_{\mathrm{SB}}$ is not negligible, and its variations along the path of the cloud could cause the changes to the cloud volume observed during the experiments.

VI. SUMMARY AND CONCLUSIONS

In this study, we have used high-speed digital in-line holography along with white light imaging to observe and measure cavitation phenomena within a high intensity focused ultrasonic beam in otherwise quiescent water. The amplitude of pressure oscillations is sufficiently high to cause changes to the water density and, consequently, to its refractive index. These changes are recorded in holograms and used to estimate the amplitude of pressure oscillations. The partially attenuated wave reflected by the container walls interferes with the primary wave giving rise to a partial standing wave, in which the pressure field consists of both traveling and standing components with clearly defined pressure nodal and antinodal regions. Clouds of cavitation bubbles typically appear first near the antinodes, and then travel at speeds of several m/s in the same direction as the primary sound wave, consistent with prior observations.[22,23] The typical cloud size is a fraction of a millimeter, much smaller than the ultrasonic beam size, and it contains hundreds of microbubbles with typical radius of 20 μm. Since the bubbles disappear in less than our fastest frame rate of 33 μs, we conclude that they contain mostly vapor. Therefore, the diffusion of non-condensable gases dissolved in the liquid does not play a significant role. The size and speed of the smaller clouds vary periodically, with the speed peaking at the nodes, and the size at the antinodes. When the cloud becomes large enough to block a significant fraction of the acoustic beam, these variations disappear. Under such conditions, after an initial growth, the cloud size and 1–2 m/s migration velocity remain approximately constant.

The cloud motion cannot be a result of acoustic streaming since it moves at speeds that are much higher than that of the liquid surrounding the cloud. To explain the observed phenomena, we have used an approximate model that accounts for the primary Bjerknes force, sound attenuation, added mass, and drag. The volumetric oscillations of the cloud, required to calculate the primary Bjerknes force, as well as the sound attenuation through the cloud, have been estimated using linearized theories. With the cloud size as an input, the model predicts fairly well the velocity magnitude and its variations along the partial standing wave. The dominant forces in the cloud dynamics are the primary Bjerknes force and the drag force. The model also predicts the cloud motion when the sound attenuation is high enough to eliminate the reflected wave.

The oscillations in cloud size, which peaks in the nodal regions, cannot be caused by spatial variations in cavitation, since the pressure oscillations peak at the antinodes. To explain them, at least qualitatively, we have considered the effect of the secondary Bjerknes force, which involves the interaction among bubbles. The force calculated using linear bubble dynamics indicates attraction among the bubbles, which increases with the magnitude of pressure oscillations and can be of the same order as the primary Bjerknes force. This attraction would reduce the cloud size around the antinodes to a greater extent than in the vicinity of the nodes, possibly explaining the observed trends.

ACKNOWLEDGMENTS

The authors would also like to thank Yuri Ronzhes for his contributions to the construction of the experimental setups.

[1] L. A. Crum, "Cavitation microjets as a contributory mechanism for renal calculi disintegration in ESWL," J. Urol. **140**(6), 1587–1590 (1988).
[2] J. J. Rassweiler, T. Knoll, K. U. Kohrmann, J. A. McAteer, J. E. Lingeman, R. O. Cleveland, M. R. Bailey, and C. Chaussy, "Shock wave technology and application: An update," Eur. Urol. **59**(5), 784–796 (2011).
[3] J. Krimmel and T. Colonius, "Numerical simulation of shock wave generation and focusing in shock wave lithotripsy," J. Acoust. Soc. Am. **123**(5), 3367–3367 (2008).
[4] Y. Matsumoto, J. S. Allen, S. Yoshizawa, T. Ikeda, and Y. Kaneko, "Medical ultrasound with microbubbles," Exp. Therm. Fluid Sci. **29**(3), 255–265 (2005).
[5] O. A. Sapozhnikov, A. D. Maxwell, B. MacConaghy, and M. R. Bailey, "A mechanistic analysis of stone fracture in lithotripsy," J. Acoust. Soc. Am. **121**(2), 1190–1202 (2007).
[6] T. Ikeda, S. Yoshizawa, M. Tosaki, J. S. Allen, S. Takagi, N. Ohta, T. Kitamura, and Y. Matsumoto, "Cloud cavitation control for lithotripsy using high intensity focused ultrasound," Ultrasound Med. Biol. **32**(9), 1383–1397 (2006).
[7] S. Yoshizawa, T. Ikeda, A. Ito, R. Ota, S. Takagi, and Y. Matsumoto, "High intensity focused ultrasound lithotripsy with cavitating microbubbles," Med. Biol. Eng. Comput. **47**(8), 851–860 (2009).
[8] A. P. Duryea, A. D. Maxwell, W. W. Roberts, Z. Xu, T. L. Hall, and C. A. Cain, "*In vitro* comminution of model renal calculi using histotripsy," IEEE Trans. Ultrason. Ferroelectr. Freq. Control **58**(5), 971–980 (2011).
[9] C. C. Coussios, C. H. Farny, G. Ter Haar, and R. A. Roy, "Role of acoustic cavitation in the delivery and monitoring of cancer treatment by high-intensity focused ultrasound (HIFU)," Int. J. Hyperthermia **23**(2), 105–120 (2007).
[10] J. Xu, T. A. Bigelow, and G. M. Riesberg, "Impact of preconditioning pulse on lesion formation during high-intensity focused ultrasound histotripsy," Ultrasound Med. Biol. **38**(11), 1918–1929 (2012).
[11] K. D. Evans, B. Weiss, and M. Knopp, "High-intensity focused ultrasound (HIFU) for specific therapeutic treatments: A literature review," J. Diagn. Med. Sonography **23**(6), 319–327 (2007).
[12] C. C. Coussios and R. A. Roy, "Applications of acoustics and cavitation to noninvasive therapy and drug delivery," Annu. Rev. Fluid Mech. **40**, 395–420 (2008).
[13] K. S. Suslick, "Sonochemistry," Science **247**(4949), 1439–1445 (1990).
[14] K. S. Suslick, Y. Didenko, M. M. Fang, T. Hyeon, K. J. Kolbeck, W. B. McNamara, M. M. Mdleleni, and M. Wong, "Acoustic cavitation and its chemical consequences," Philos. Trans. R. Soc. London, Ser. A **357**(1751), 335–353 (1999).
[15] M. Hauptmann, F. Frederickx, H. Struyf, P. Mertens, M. Heyns, S. De Gendt, C. Glorieux, and S. Brems, "Enhancement of cavitation activity and particle removal with pulsed high frequency ultrasound and supersaturation," Ultrason. Sonochem. **20**(1), 69–76 (2013).
[16] P. A. Deymier, J. O. Vasseur, A. Khelif, B. Djafari-Rouhani, L. Dobrzynski, and S. Raghavan, "Streaming and removal forces due to second-order sound field during megasonic cleaning of silicon wafers," J. Appl. Phys. **88**(11), 6821–6835 (2000).
[17] Z. Eren, "Ultrasound as a basic and auxiliary process for dye remediation: A review," J. Environ. Manage. **104**, 127–141 (2012).
[18] T. G. Leighton, A. J. Walton, and M. J. W. Pickworth, "Primary Bjerknes forces," Eur. J. Phys. **11**, 47–50 (1990).
[19] J. Rensen, D. Bosman, J. Magnaudet, C. D. Ohl, A. Prosperetti, R. Togel, M. Versluis, and D. Lohse, "Spiraling bubbles: How acoustic and hydrodynamic forces compete," Phys. Rev. Lett. **86**(21), 4819–4822 (2001).
[20] A. A. Doinikov, "Translational motion of a spherical bubble in an acoustic standing wave of high intensity," Phys. Fluids **14**(4), 1420–1425 (2002).
[21] C. E. Brennen, "Fission of collapsing cavitation bubbles," J. Fluid Mech. **472**, 153–166 (2002).
[22] G. W. Willard, "Ultrasonically induced cavitation in water—A step-by-step process," J. Acoust. Soc. Am. **25**(4), 669–686 (1953).
[23] C. Wu, N. Nakagawa, and Y. Sekiguchi, "Observation of multibubble phenomena in an ultrasonic reactor," Exp. Therm. Fluid Sci. **31**(8), 1083–1089 (2007).
[24] A. D. Maxwell, T. Y. Wang, C. A. Cain, J. B. Fowlkes, O. A. Sapozhnikov, M. R. Bailey, and Z. Xu, "Cavitation clouds created by shock scattering from bubbles during histotripsy," J. Acoust. Soc. Am. **130**(4), 1888–1898 (2011).
[25] M. Arora, C. D. Ohl, and D. Lohse, "Effect of nuclei concentration on cavitation cluster dynamics," J. Acoust. Soc. Am. **121**(6), 3432–3436 (2007).
[26] Y. Lu, J. Katz, and A. Prosperetti, "Generation and transport of bubbles in intense ultrasonic fields," in *Proceedings of the ASME 2012 Fluids Engineering Summer Meeting, Rio Grande, Puerto Rico, 8–12 July 2012* (ASME, 2012), Paper No. FEDSM2012-72286.
[27] J. Katz and J. Sheng, "Applications of holography in fluid mechanics and particle dynamics," Annu. Rev. Fluid Mech. **42**, 531–555 (2010).
[28] J. H. Milgram and W. C. Li, "Computational reconstruction of images from holograms," Appl. Opt. **41**(5), 853–864 (2002).
[29] J. Sheng, E. Malkiel, and J. Katz, "Digital holographic microscope for measuring three-dimensional particle distributions and motions," Appl. Opt. **45**(16), 3893–3901 (2006).
[30] Y. Lu, B. Gopalan, E. Celik, J. Katz, and D. M. Van Wie, "Stretching of turbulent eddies generates cavitation near a stagnation point," Phys. Fluids **22**(4), 041702 (2010).
[31] F. Dubois, L. Joannes, and J. C. Legros, "Improved three-dimensional imaging with a digital holography microscope with a source of partial spatial coherence," Appl. Opt. **38**(34), 7085–7094 (1999).

[32] U. Schnars and W. Juptner, "Direct recording of holograms by a CCD target and numerical reconstruction," Appl. Opt. **33**(2), 179–181 (1994).
[33] W. B. Xu, M. H. Jericho, I. A. Meinertzhagen, and H. J. Kreuzer, "Digital in-line holography for biological applications," Proc. Natl. Acad. Sci. U.S.A. **98**(20), 11301–11305 (2001).
[34] R. J. Goldstein, *Fluid Mechanics Measurements* (Taylor & Francis, Philadelphia, 1996).
[35] I. Thormahlen, J. Straub, and U. Grigull, "Refractive-index of water and its dependence on wavelength, temperature, and density," J. Phys. Chem. Ref. Data **14**(4), 933–946 (1985).
[36] C. E. Brennen, *Fundamentals of Multiphase Flow* (Cambridge University Press, New York, 2005).
[37] M. P. Brenner, S. Hilgenfeldt, and D. Lohse, "Single-bubble sonoluminescence," Rev. Mod. Phys. **74**(2), 425–484 (2002).
[38] L. A. Crum, "Bjerknes forces on bubbles in a stationary sound field," J. Acoust. Soc. Am. **57**(6), 1363–1370 (1975).
[39] J. R. Hong, J. Katz, and M. P. Schultz, "Near-wall turbulence statistics and flow structures over three-dimensional roughness in a turbulent channel flow," J. Fluid Mech. **667**, 1–37 (2011).
[40] M. S. Plesset and A. Prosperetti, "Bubble dynamics and cavitation," Annu. Rev. Fluid Mech. **9**, 145–185 (1977).
[41] W. Kreider, L. A. Crum, M. R. Bailey, and O. A. Sapozhnikov, "A reduced-order, single-bubble cavitation model with applications to therapeutic ultrasound," J. Acoust. Soc. Am. **130**(5), 3511–3530 (2011).
[42] L. Dagostino and C. E. Brennen, "Linearized dynamics of spherical bubble clouds," J. Fluid Mech. **199**, 155–176 (1989).
[43] K. W. Commander and A. Prosperetti, "Linear pressure waves in bubbly liquids—Comparison between theory and experiments," J. Acoust. Soc. Am. **85**(2), 732–746 (1989).
[44] Y. Hao and A. Prosperetti, "The dynamics of vapor bubbles in acoustic pressure fields," Phys. Fluids **11**(8), 2008–2019 (1999).
[45] V. N. Alekseev, "Steady-state behavior of a vapor bubble in an ultrasonic-field," Sov. Phys. Acoust. **21**(4), 311–313 (1975).
[46] L. Dagostino and C. E. Brennen, "Acoustical absorption and scattering cross-sections of spherical bubble clouds," J. Acoust. Soc. Am. **84**(6), 2126–2134 (1988).
[47] J. Lighthill, *Waves in Fluids* (Cambridge University Press, Cambridge, UK, 1978).
[48] J. Lighthill, "Acoustic streaming," J. Sound Vib. **61**(3), 391–418 (1978).
[49] F. W. Roos and W. W. Willmarth, "Some experimental results on sphere and disk drag," AIAA J. **9**(2), 285–291 (1971).
[50] H. Lamb, *Hydrodynamics* (Dover Publications, New York, NY, 1945).